Applied Optics (Lasers, Photonics, and Environmental Optics) 39 (27) 5-23-5030

LIGHT SCATTERING FROM DEFORMED DROPLETS AND DROPLETS WITH INCLUSIONS. I: EXPERIMENTAL RESULTS

David R Secker, Paul H Kaye, Richard S Greenaway, Edwin Hirst,

Science and Technology Research Centre, University of Hertfordshire, Hatfield, AL10 9AB, U.K

David L. Bartley,

National Institute for Occupational Safety and Health, NIOSH, Cincinnati, Ohio.

and Gorden Videen.

Army Research Laboratory, Adelphi, MD.

ABSTRACT

This is the first part of a two-part paper dealing respectively with experimental and theoretical results from the scattering of light by deformed liquid droplets and droplets with inclusions. Characterizing droplet deformation could lead to improved measurement of droplet size as measured by commercial aerodynamic particle sizing instruments. Characterizing droplets with inclusions can be of importance in some industrial, occupational, and military aerosol monitoring scenarios. The nozzle assembly from a TSI Aerodynamic Particle Sizer was used to provide the accelerating flow conditions in which experimental data were recorded. A Helium Neon laser was employed to generate the light scattering data and an externally triggered, pulsed Copper Vapor laser provided illumination for a droplet imaging system arranged orthogonal to the HeNe scattering axis. The observed droplet deformation correlates well over a limited acceleration range with theoretical predictions derived from analytical solution of the Navier-Stokes equation.

OCIS codes 290.0290 scattering

290.5820 scattering measurements

290.5850 scattering, particles.

INTRODUCTION

The authors are currently investigating light scattering methods which could be used to correct for the errors which are known to occur in the measurement of liquid droplets by commercial aerodynamic particle sizing instruments. In carrying out the investigation, it became apparent that the apparatus used for droplet deformation studies was also capable of reproducibly generating droplets with inclusions. These are of importance since they can be representative of aerosols found in hospital or battlefield environments where biological organisms can survive for prolonged periods when contained within a protective liquid coat. This paper therefore describes the acquisition of experimental light scattering data from both deformed droplets and droplets with inclusions. These data may be used to help develop and test theoretical inversion algorithms, some of which are described in Part II of the paper, which could ultimately allow rapid characterization and/or identification of these droplet morphologies. This in turn could lead to improvements in commercial aerodynamic particle sizers and new opportunities for the development of light scattering aerosol monitoring instruments for bio-aerosol detection.

Aerodynamic Particle Sizers

The size of an airborne droplet may be defined in a number of ways depending on the method of measurement. However, in studies of therapeutic aerosol sprays, combustion aerosols, paint sprays and coatings, where on-line or real-time measurements are required and/or where the airborne behaviour of the droplet is relevant to the application, the aerodynamic size, d_a, is frequently sought. d_a is defined as the diameter of a unit density sphere having the same gravitational-settling velocity as the particle in question. The traditional method of determining the aerodynamic size of a particle was by measuring its gravitational settling velocity using suitable sedimentation instruments. This process was slow and laborious and commercial instruments based on the acceleration of particles were developed as an alternative [1]. The most widely used commercial aerodynamic sizers are the TSI APS family of

instruments (3300 series, TSI Inc., St Paul, MN), which achieve the desired particle size measurement by accelerating a sample airstream in which the particles are suspended and measuring the velocity acquired by individual particles. The larger particles exhibit greater inertia and thus accelerate more slowly, thereby attaining lower velocities. In the APS instruments, an aerodynamic accelerating nozzle, in which a sample flow is sheathed in filtered air, produces the necessary accelerating flow, as illustrated in Figure 1. The total airflow through the nozzle is regulated to 5l/min, 4l/min of which is filtered to provide the sheath flow. The time-of-flight of the particle through two closely spaced laser beams positioned a few hundred micrometres beneath the nozzle exit is recorded from the pulses of light scattered by the particle to an optical detector. An assessment of the particle's aerodynamic size is determined by relating the transit time to an internal calibration function based upon measured times of flight of solid spherical calibration particles. The size range covered by this instrument is from 0.5μm to 30μm aerodynamic diameter, depending on the instrument model used.

However, aerodynamic sizing instruments of this type suffer a significant limitation in that the measured aerodynamic size can be significantly affected by particle shape. When attempting to measure non-spherical particles of known density, the shape (and orientation) of each particle subjected to the accelerating air-flow governs the drag force it experiences and hence affects the measured aerodynamic size. The measurement of liquid aerosol droplets is subject to significant error (25% under-sizing reported in some cases) because the droplets deform to oblate spheroids in the accelerating airflow. As a result of this deformation, their cross-sectional area increases and they experience a greater acceleration than would be the case with similar sized rigid spheres. Despite being well reported in the past by Baron [2] and Griffiths *et al* [3], there is as yet no systematic method of measuring the degree of deformation experienced by individual droplets in the instrument and material specific calibration curves, derived for example using gravitational settling techniques, are invariably required.

Spatial Light Scattering

The spatial distribution of light scattered by a particle, also in certain texts referred to as the TAOS (Two-dimensional Angular Optical Scattering) pattern [4], is a complex function of the size, shape, dielectric structure, and orientation of the particle, as well as of the properties of the illuminating radiation (wavelengths, polarization state). Analysis of the scattering pattern can provide a means of characterizing the shape, orientation, and internal structure of the illuminated particle and many workers have exploited this property in various ways. Previous work by the authors [5] has explored the potential of scattering pattern analysis for particle shape and size classification and has demonstrated [6,7] how such techniques may be implemented in real-time airborne particle measurement systems designed for ambient aerosol characterization and asbestos fiber detection.

Scattering patterns can cover different scattering angle ranges depending on the light collection geometry used to acquire them. The examples shown in Figure 2 (see Figure caption for description of particle types) were recorded by imaging the pattern of light scattered by individual particles onto an intensified charge-coupled device (ICCD) camera as the particles were carried by an airstream through a laser beam. The particle transition time through the beam was ~2 μs and in each case light scattered between 5° and 30° scattering angle and throughout 360° of azimuth was captured as a 256 by 256 pixel image. The beam direction is perpendicular to the paper into the center of each image. Each white dot in the patterns corresponds to a single scattered photon and the images thus represent photon distribution maps of several thousands to several tens of thousands of scattered photons. The images illustrate the wide variations these patterns can assume for different particle shapes and orientations. It was the potential of spatial light scattering analysis for real-time particle shape characterization that initiated the fundamental study of droplet scattering reported here. It also underpins an ultimate aim of this work, namely to provide an on-line optical means of correcting for the errors in measured aerodynamic size caused by droplet deformation in instruments such as the APS3300 series.

APPARATUS

An apparatus was constructed which allowed the acquisition of both spatial scattering patterns and real images from individual droplets in the sub-30μm size range as they traversed the measurement space below an APS3320 sample delivery nozzle (donated by TSI Inc.). The apparatus is shown schematically in Figure 3. As stated earlier, the actual TSI APS3300 series of instruments incorporate two closely spaced cross-polarized beams and measure particle time-of-flight between the beams. However, for the fundamental results reported here the spatial light scattering pattern images were produced using a single beam from a 633nm 15mW plane polarized Helium-Neon laser (model 05-LHP-151, Melles Griot Inc., Carlsbad, CA). Furthermore, whilst the normal operating flow-rate of the TSI APS instrument is 5 l/min (comprising 1 l/min sample flow-rate and 4 l/min of filtered sheath flow), we have additionally observed droplet behaviour over a range of flow conditions both less than and greater than the norm so as to gain a greater understanding of the morphological changes taking place.

Light Scattering Pattern Acquisition

The beam from the HeNe laser passes through a quarter-wave plate to render the light circularly polarized before being focused through a cylindrical lens to produce a beam of elliptical cross-section (approximately 1.2mm by 100μm) at the point of intersection with the sample air flow. Monodisperse droplets are generated into the sample flow using a Vibrating Orifice Aerosol Generator, VOAG (TSI Inc., St. Paul, MN) as described below. As each droplet traverses the beam, light scattered in the forward direction between angles of 5° and 20° is imaged onto an intensified, asynchronously triggered ICCD camera (ICCD225, Photek Ltd., East Sussex, U.K.). The lower angular limit is set by a beam-stop, whilst the higher limit is set so as to avoid shadowing of the scattered light by the lower surface of the sample

delivery nozzle. Images from the camera are digitized, displayed, and stored on a computer at a rate of several images per second, for later analysis. A trigger signal for the acquisition of a scattering pattern by the camera is derived from a separate photomultiplier detector module which receives light scattered at a higher scattering angle than the camera, as indicated in Figure 3. The rising and trailing edges of the signal from the photomultiplier detector respectively initiate and terminate the camera integration period, this being typically ~2μs duration.

Droplet Image Acquisition

Real images of the droplets are acquired using a CCD camera assembly mounted orthogonal to the HeNe scattering axis. In the manner first described by Baron [3][8], the droplets are viewed against a bright diffusing screen. The illumination for this screen is derived from a Copper Vapor laser (Oxford Lasers Ltd., U.K.)that delivers pulses of 38ns duration at wavelengths of 510nm and 578nm. Each pulse has an energy of approximately 2mJ. Again, appropriate triggering of the laser pulses is achieved by use of the signal from the photomultiplier detector. The imaging system uses a high numerical aperture microscope objective lens and a standard microscope tube resulting in an overall image magnification of approximately x10. A digital non-intensified CCD camera (model KP-F100, Hitachi Denshi Ltd. Tokyo, Japan) was used to acquire images as this offered both high read-out speed and small pixel size (6.7μm square). This pixel size produced images of acceptable resolution, the diameter of a 20μm droplet for example covering approximately 30 pixels within a 1,300 x 1,030 pixel image. A Foucault knife-edge test [9] was performed to determine the resolution of 3 pixels for the image quality attainable with this configuration.

It was originally intended to acquire scattering patterns and real images simultaneously from the same droplet. This would have required appropriate optical filtering to prevent the intense illumination from the Copper Vapor laser reaching the intensified ICCD camera. However, the fact that the pulsed radiation was

broad-field (as a result of the diffusion screen) and multi-wavelength, made the task of attenuating this radiation to a degree sufficient to prevent damage to the ICCD camera extremely difficult without significantly attenuating the 633 nm scatter light flux also. Fortuitously, the uniformity of droplet size produced by the VOAG for a given set of generating conditions was such that the scattering patterns and images from successive droplets were remarkably reproducible, the differences being principally a result of the optical quantization noise. It was therefore decided to avoid potential over-illumination of the ICCD by recording the scattering patterns and real droplet images from successive droplets rather than the same droplet, ensuring that the ICCD was disabled during the firing of the pulsed laser.

Droplet Generation and Delivery

The VOAG produces droplets by inducing mechanical instability in a fine liquid jet through excitation with a piezo-electric oscillator. When first formed droplets are comparatively large and comprise a solute, in our case either oleic acid or glycerol, in solution with AR grade iso-propyl alcohol. Dry (<1%RH) compressed air is used to transport the droplet aerosol from the VOAG drying column to the light scattering instrument, during which time the alcohol evaporates to leave pure oleic acid or glycerol droplets. A bleed valve controls the total flow-rate through the nozzle subsystem. For the experiments described, the total flow-rate was set prior to the acquisition of scattering data and the sheath air flow-rate was measured prior to and during acquisition using a bubble flow meter. The measured sample flow-rate was found to be consistently 20% of the total flow-rate and was found to be stable to within 1% during the period of experimental data acquisition.

EXPERIMENTAL DATA

All experimental data presented here were recorded from oleic acid droplets, with the exception of that shown in Figure 8b which shows scattering from a glycerin droplet. Figure 4 illustrates the changes

which occur in the spatial light scattering patterns from individual droplets as a function of both droplet size and increasing sample flow-rate. Each scattering pattern was recorded over a 2μs period as the droplet traversed the HeNe beam beneath the aerosol delivery nozzle. Each scattering pattern therefore represents the forward scattering from a deformed droplets illuminated at 90° to its axis of symmetry. The images on the top row were recorded from 8μm diameter droplets at total flow-rates from 1 l/min to 6 l/min respectively. Subsequent rows show the scattering behaviour of 12μm, 16μm, 20μm, 25μm and 30μm diameter droplets for similar values of flow-rate. The gain of the image intensifier was reduced for larger droplet sizes (and/or lower droplet velocities) to minimize optical saturation effects, although these are still present as extended solid white areas in some of the larger droplet/lower velocity patterns. Ananth and Wilson [10] have carried out a theoretical analysis of the gas and particle velocities present in the APS delivery nozzle. Their results predict that at the normal APS operational flow-rate of 5 l/min the gas velocity at the measurement point is approximately 160 m/s and the velocity of a 10 μm spherical particle is approximately 50 m/s.

At the lowest flow-rate and smallest droplet size (top-left image) the scattering pattern correlates closely with that predicted by Mie theory [11] for a perfect sphere. No droplet deformation is discernible from the light scattering data in this image. For increasing flow-rate and/or droplet size, however, the degree of droplet deformation is evident from the increasing ellipticity of the scattering maxima and minima evident on the patterns. This behaviour appears well behaved until a point is reached such as at image ’16 μm dia: 5 l/min’ at which bright horizontal barring occurs on the image. This is predicted by the theoretical analysis described in Part II of this paper [12]. This barring may occur either as a predominant central white bar or as a series of parallel horizontal scattering fringes as on image ’20 μm dia: 5 l/min’. Increasing the flow-rate or droplet size further results in more complex interference patterns within the images, such as on image ’30 μm dia: 5 l/min’. This behaviour appears to indicate that the droplets are

undergoing a transition from simple oblate spheroidal form to the more complex morphologies as first observed by Baron [2]. It also indicates that the task of attempting to rapidly assess the deformation of a single droplet by analysis of its light scattering pattern (as we desire for on-line correction of deformation effects in aerodynamic sizing) is non-trivial for droplets deformed beyond a certain degree.

Figure 5 shows light scattering pattern images for undistorted droplet diameters of 20 μm, 25 μm, and 30μm, and total flow-rates from 1 to 6 l/min. Adjacent to each scattering pattern is the corresponding droplet image. These latter images indicate the changes in droplet shape that produce the increasingly complex scattering data. The essentially perfect spheres undergo flattening into oblate spheroids, then become biconcave discs before forming menisci having concave upper surfaces. This morphological transition coincides with the dominant feature of the respective scattering patterns changing from a horizontal to a vertical bright band, the former possibly the result of a morphology dependent resonance in the droplet, and the latter a function of the increasingly narrow horizontal cross-section which the droplet presents. We are currently investigating these effects further with the hope of elucidating the causes of the dominant scattering features.

QUANTIFYING DROPLET DEFORMATION

Inversion of the light scattering data to yield droplet deformation descriptors is dealt with in Part II of this paper [12]. As a comparative measure, a first-order estimate of droplet deformation under given flow conditions may be obtained from the Feret ratio (Fr) of the droplet image, defined as the ratio of Feret diameters, i.e. maximum distances between particle edges in the x and y directions of the image (i.e. orthogonal to and parallel to the particle trajectory respectively). The edges of the droplets E(x,y) were determined by a computer-based Gaussian edge detection algorithm [13]. The threshold value for this

algorithm can be set manually or left to be determined automatically from the background intensity. Since the background intensity is different for each image, the automatic threshold function was employed. In addition, the graininess of the background can make the algorithm detect erroneous edges in the background. However, the algorithm generally provides a continuous line that is evident as an edge in the binary file that the algorithm creates. The Feret ratio can then be determined from this binary file. Figure 6 shows a plot of Feret ratio vs. flow-rate for 20 μm oleic acid droplets. As can be seen from the Figure, the Feret ratio is well behaved up to 4.5 l/min. flow-rate. The reduction in the rate of increase of the Feret ratio immediately after this point coincides with the droplet beginning to assume a meniscus form (see Figure 5), for which the Feret ratio is less. The change in the curve at 4.5 l/min flow-rate coincides with the point at which the horizontal banding appears in the scattering pattern. A significant part of the experimental uncertainty in the Feret ratio measurements is caused by blurring of the droplet images in the direction of motion, especially at higher flow-rates. Methods to minimize motion blur by reducing the laser pulse width are currently being explored.

Analytical Solution of Droplet Deformation

Liquid droplet distortion produced in an accelerating flow field has been computed through analytical solution of the Navier-Stokes equation by Bartley *et al* [14], and this has lead to a means of correlating observed droplet deformation to parameters such as droplet diameter, viscosity, surface tension, and density. A high Reynolds number empirical approximation to the pressure external to the droplet has been used in these calculations. This procedure, described in detail by Bartley *et al* [ibid], correctly predicts the change in droplet shape with increasing flow-rate from spherical to spheroidal to biconcave disc. For example, Figure 7 shows the image of a 20μm nominal diameter oleic acid droplet together with the corresponding computed cross-section. Beyond this level of distortion, the theoretically computed shape pattern is not reliable.

DROPLETS WITH INCLUSIONS

During the process of collecting experimental light scattering and particle image data of the type described earlier, a phenomenon was observed which has since been attributed to the presence of inclusions in the observed liquid droplets. This is of potential interest because droplets with internal bodies may occur in environments such as hospital buildings where entities such as biological organisms can remain viable over long periods by encapsulation within liquids. Similar conditions can apply in the dispersal of biological warfare agents. As a consequence, there is interest in theoretically modeling the light scattering behaviour of such two-component droplets with the object of ultimately establishing a means of recognizing their presence in an environment. Reproducible experimental data from droplets with inclusions can thus provide a valuable resource for verifying theoretical inversion methods.

As stated earlier, the VOAG droplets are normally generated into a dry atmosphere, typically <1%RH. When 20 μm droplets of glycerin, in which water is soluble, were generated into a moist atmosphere at 40%RH, no perturbations of the expected scattering patterns were observed (see Figure 8a). However, when similar sized droplets of oleic acid, in which water is insoluble, were generated into the same atmosphere, light scattering patterns of the type shown in Figure 8b were consistently observed. These preliminary scattering data were recorded at a flow-rate of 1 l/min.

The striking feature of the oleic acid pattern is the displaced secondary scattering fringes superimposed on the normal concentric rings from a homogeneous sphere. Figure 8c shows a droplet image from the same oleic acid aerosol (though, for the reasons given the section Droplet Image Acquisition, not from the same droplet as Fig. 8b), and this clearly shows the presence of an internal dielectric discontinuity. The position of the secondary scattering fringes relative to those from the host droplet provides good evidence to support the hypothesis of an inclusion offset vertically upwards from the center of the oleic acid host, and

again this is supported both by the reproducibility of the images of the droplets (such as Fig. 8c) and by theoretical analysis [12]. The cause of this upward shift of the inclusion within the host may reasonably be assumed to be due to the density difference between the inclusion and host, as is the case with water and oleic acid (0.998 g/cm^3 cf. 0.895g/cm^3). The higher density water inclusion moves towards the top of the host oleic acid droplet when the droplet is accelerated downwards within the airflow through the APS delivery nozzle.

These results are preliminary, and the exact mechanism by which the water inclusion is created is not yet known. One hypothesis is that water vapor condenses onto the original droplets and dissolves into the alcohol present. Once the alcohol has evaporated, the water, which has a higher surface tension than oleic acid, forms a single droplet enveloped by the oleic acid. To thermodynamically model such a system is complex but has been the subject of recent work by other authors [15][16]. For smaller host droplet sizes, the secondary scattering becomes distorted to yield downward bright arms as shown in Figure 9. Theoretical analysis [12] suggests that this change in scattering is commensurate with an increase in the size of the inclusion relative to the host.

DISCUSSION

The experimental data presented in this paper illustrate the complex spatial light scattering behaviour of droplets distorted by accelerating flow fields and droplets containing inclusions. These data are, we believe, the first of their type to be reported. The reproducibility of the experimental data makes them a valuable resource in the development and testing of theoretical inversion models. Such models may ultimately provide a route to the rapid characterization and/or identification of complex droplet morphologies and this in turn could lead to advances in instrumentation for droplet aerodynamic sizing and for the detection of potential bio-aerosol hazards in hospital and battlefield situations. In Part II of this paper, numerically calculated spatial light scattering data are presented which indicate that theoretical

inversion of the light scatter data is achievable for a variety of droplet morphologies relevant to the experimental conditions described above.

ACKNOWLEDGEMENTS

This work was carried out with funding from the UK Engineering and Physical Sciences Research Council (grant GR/L33375), the National Institute of Occupational Safety and Health, and with generous support from TSI Inc. St. Paul. MN.

REFERENCES

[1] J. K. Agarwal, and R. J. Remiarz, "Development of an aerodynamic particle size analyser", USDHEW-NIOSH Contract Report No. 210-80-0800, Cincinnati OH: NIOSH (1981).

[2] P. A. Baron, "Calibration and use of the Aerodynamic Particle Sizer (APS 3300)," *Aerosol Sci. Technol.*, **5**, 55-67 (1986).

[3] W. D. Griffiths, P. J. Iles, and N. P. Vaughan, "The behaviour of liquid droplets in an APS 3300," *J. Aerosol Sci.*, **17**, 427-431 (1986).

[4] S. Holler, Y. Pan, R. K. Chang, J. R. Bottiger, S. C. Hill and D. B. Hillis, "Two-dimensional angular optical scattering for the characterization of airborne microparticles", *Optics Letters* **23,** 18, 1489-1491 (1998).

[5] E Hirst, P H Kaye, and J R Guppy, "Light scattering from non-spherical airborne particles; theoretical and experimental comparisons". *Applied Optics* **33**, (30), 7180-7187 (1994).

[6] P.H. Kaye, K. Alexander-Buckley, E. Hirst, and S. Saunders "A real-time monitoring system for airborne particle shape and size analysis"**,** *J. Geophysical Res. (Atmospheres),* **101**, D14, 19,215-19,221 (1996).

[7] P. H. Kaye, E. Hirst, and Z. Wang-Thomas, "Neural-network based spatial light-scattering instrument for hazardous airborne fiber detection," *Applied Optics*, **36**, 6149-6156 (1997).

[8] K. Willeke and P. A. Baron, *Aerosol Measurement: principles, techniques, and applications*. (New York: Van Nostrand Reinhold, 1993).

[9] W. J. Smith, *Modern Optical Engineering*, 439-443 (New York: McGraw-Hill, 1966).

[10] G. Ananth and J. C. Wilson, "Theoretical analysis of the performance of the TSI Aerodynamic Particle Sizer", *Aerosol Sci. Technol.*, **9**, 189-199 (1988).

[11] C. F. Bohren and D. R. Huffman, *Absorption & Scattering of Light by Small Particles.* (Wiley-InterScience, New York, 1983).

[12] G. Videen, W. Sun, Q. Fu, D. R. Secker, P. H. Kaye, R. S. Greenaway, E. Hirst, and D. L. Bartley, "Light scattering from deformed droplets and droplets with inclusions. II: Theoretical treatment", *Applied Optics* (this issue).

[13] Matlab, 5.3.0.10183 (R11), The Mathworks, Inc., 3 Apple Drive, Natick, Mass. 01760 (1999).

[14] D. L. Bartley, A. B. Martinez, P. A. Baron, D. R. Secker, and E. Hirst, "Droplet distortion in accelerating flow". *J. Aerosol Science*,(accepted for publication) March 2000.

[15] T. Vesala, M. Kulmala, R. Rudolf, A. Vrtala, and P. E. Wagner, "Models for condensational growth and evaporation of binary aerosol particles," *J. Aerosol Sci*. **28**, 565-598 (1997).

[16] T. Mattila, M. Kulmala, and T. Vesala, "On the condensational growth of a multicomponent droplet," *J Aerosol Sci.*,. **28**, 553-564 (1997).

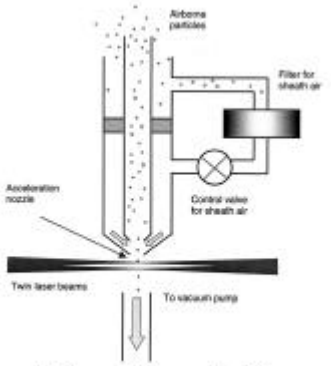

Fig. 1. Schematic diagram of the particle delivery system used in TSI APS 3300 series instruments.

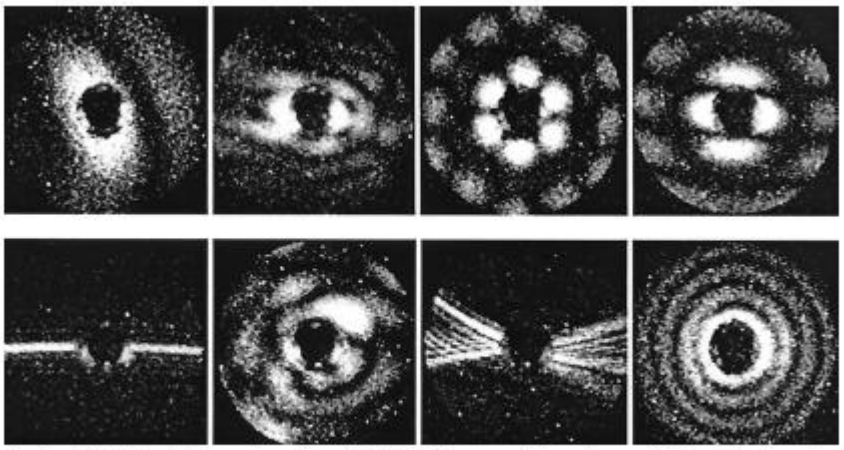

Fig. 2. Examples of spatial light-scattering patterns from individual airborne particles. Top row, left to right: hematite ellipsoid, 2 μm; copper flake, ~5 μm; sodium chloride crystal; sodium chloride crystal. Bottom row, from left to right: asbestos fiber (crocidolite); irregular background particle; asbestos fiber (chrysotile); water droplet, ~9 μm in diameter.

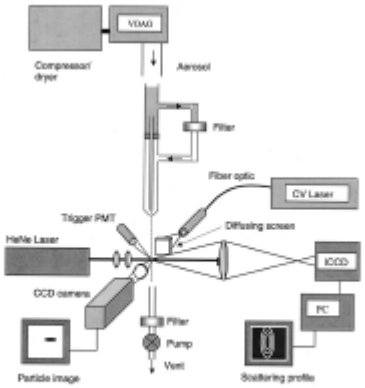

Fig. 3. Schematic diagram of apparatus used to acquire scattering patterns and real images from individual airborne droplets. PMT, photomultiplier tube; CV, copper vapor.

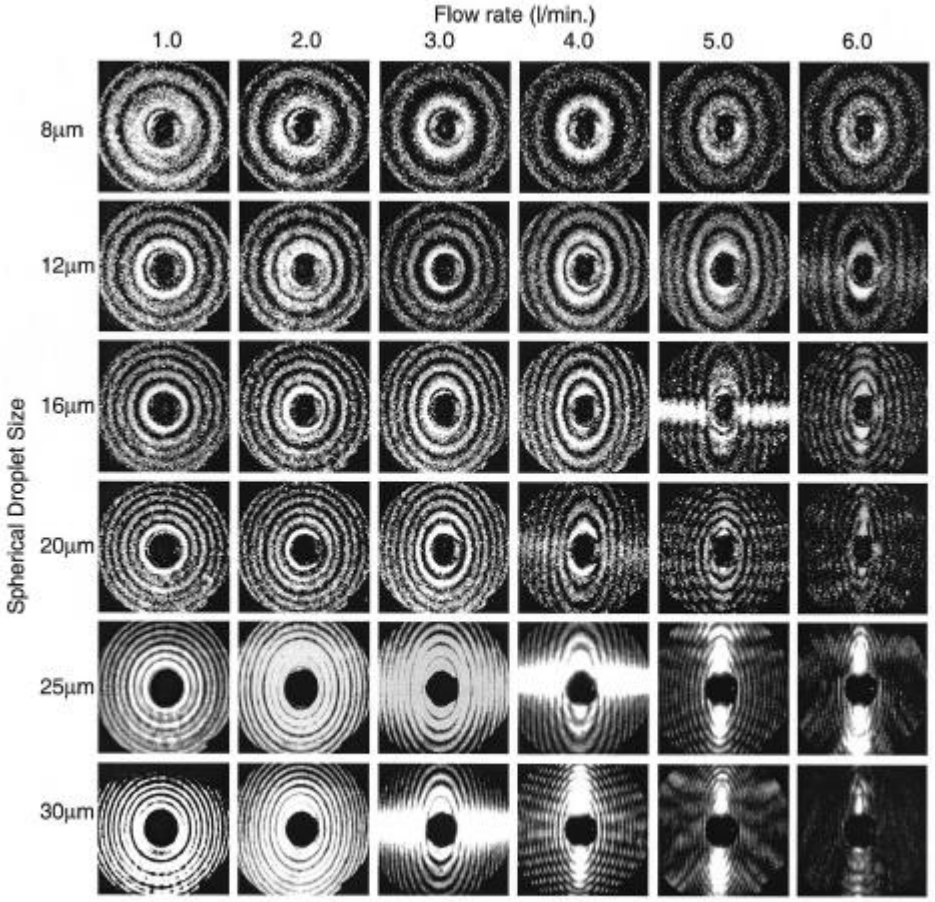

Fig. 4. Spatial light-scattering patterns from individual droplets as a function of droplet size and sample flow rate.

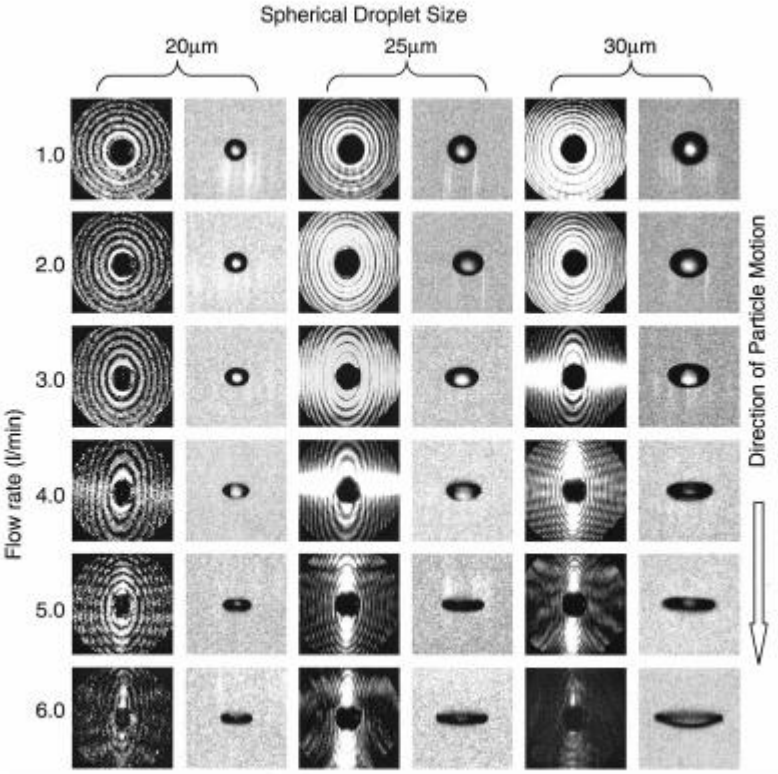

Fig. 5. Spatial light-scattering patterns and droplet images for 20-, 25-, and 30-µm-diameter droplets at various sample flow rates through the APS aerosol delivery nozzle.

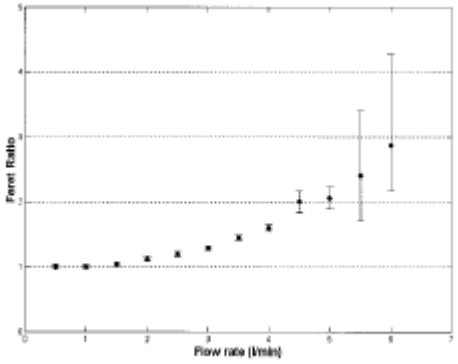

Fig. 6. Feret ratio plotted as a function of flow rate for 20-µm oleic acid droplets.

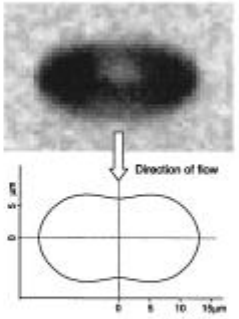

Fig. 7. Image of a 20-µm nominal diameter oleic acid droplet together with the corresponding computed cross-sectional shape. The computation used the following values: density, 0.90 g/cm^3; viscosity, 0.256 P; surface tension, 32 mJ/m^2.

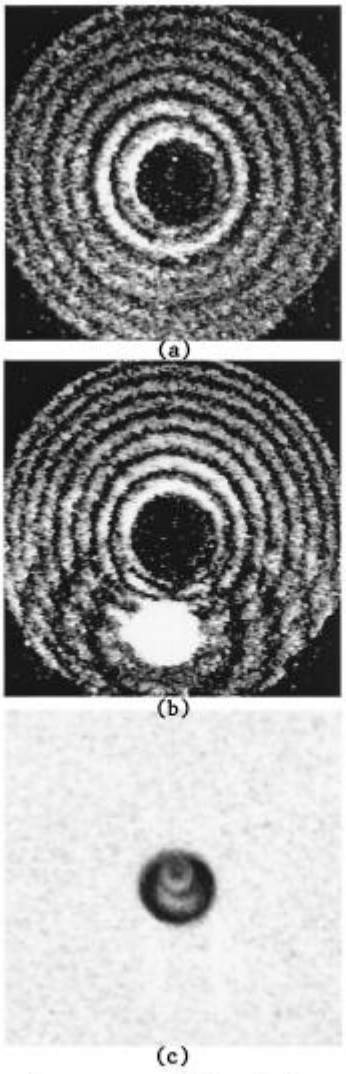

Fig. 8. Scattering patterns recorded from droplets generated in a 40% RH environment: (a) a 20-μm-diameter glycerin droplet with no inclusion and (b) a 20-μm oleic acid droplet with inclusion. (c) shows an image of the type of droplet giving rise to the scattering in (b).

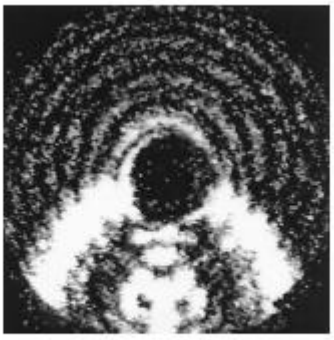

Fig. 9. Scattering pattern and image of a 16-μm-diameter oleic acid droplet containing an inclusion with greater size (relative to the host droplet) than that shown in Fig. 8.